Correctly computing targeting efficiency in magnetically targeted delivery from particle tracking models

Nina Podoliak, Giles Richardson

Mathematical Sciences, University of Southampton, Southampton, SO17 1BJ, UK

December 13, 2021

Abstract

Magnetic targeted therapies have been shown to be very effective at treating tumours in animal models (*e.g.* [22]), but have yet to be widely adopted in a clinical setting. The aim of this work is to correct a widely occurring, but subtle, error in the interpretation of models of magnetically targeted delivery. This can result in inaccuracies in the predicted targeting efficiency of up to an order of magnitude. In order to correct this error a model for magnetic targeting that is based upon a particle conservation law is developed. The close relationship between this model and the standard approach is demonstrated. Interpretation of magnetic particle dynamics in terms of a conservation law leads to an improved understanding of the overall process and results in an alternative, and correct, definition of the targeting efficiency. The particle conservation law approach is illustrated by considering targeting in a flow through a simple network, consisting of a vessel that branches into two daughter vessels, and compared to the standard procedure for computing targeting efficiency, which is based solely on a count of representative particle trajectories. It is shown that the analysis based on the conservation law yields a prediction that compares much more favourably to the results of simple *in-vitro* experiments performed in this set-up [29] than the standard, but erroneous, approach based on counting particle trajectories. The method of computing targeting efficiency that is developed here, has wider applicability and can, for example, be applied to targeting in complex mammalian vasculatures.

1 Introduction

Magnetic targeting is a non-invasive method to deliver medical therapies to specific sites in the body. It works by (i) attaching the therapeutic agent (*e.g.* drugs, genes or onco-viruses) to the magnetic nanoparticles (MNPs), typically via a functionalized carboxyl group [24], (ii) injecting the MNPs into the circulation and (iii) directing them to the target site by application of a suitable magnetic field [5, 33]. Its aims are to increase therapeutic efficiency and reduce unwanted side effects by concentrating the therapeutic agent in the target tissue and reducing the total systemic dose required by the treatment. The method has been successfully applied to delivery of chemotherapy [25] and cell therapy [22] to tumours, stem cells to injury sites [14, 28] and drugs through the blood-brain barrier [13]. It is particularly suited to delivery of therapeutic agents to tumours, because it relies on a transport vector (a magnetic nano-particle), that is too large to extravasate in healthy vasculature but which can nevertheless easily extravasate in compromised tumour vasculature. This effect, termed the enhanced permeability and retention (EPR) effect, is reviewed in [17].

The first clinical trials of magnetic targeting used permanent magnets attached to the body to provide the targeting field. While this is effective for treating surface tumours [15] it proves ineffective for targeting sites in deep tissues, since the magnetic field gradient used to target the MNPs decays rapidly with distance from the magnet [9]. An alternative, more powerful approach, is to use the magnetic field gradient coils of a Magnetic Resonance Imaging (MRI) system [25, 22, 29]. The notable advantages of this approach are the high magnetic field strengths that can be obtained, the precise temporal and three-dimensional spatial control over magnetic field gradients, and the possibility of simultaneous high contrast imaging of the surrounding tissues.

To predict the efficacy of magnetic targeting, a number of theoretical and numerical models have been developed. Most of these rely on simulating individual particles trajectories in response to the applied magnetic field and vascular flow. The simplest approaches consider non-interacting magnetic particles inside simple vessel geometries [29, 20, 27, 30, 2, 1]. More complex models account for branching vascular networks [10, 11, 31], pulsatile vascular flow [16], particle-particle interactions [11, 35, 12], shear-induced diffusion [9, 26], interactions between particles and red blood cells [7, 4, 6], particle-vessel wall interactions [23], and penetration of particles through vessel walls and tumor tissues [18, 32]. These complex models typically require that a numerical approach is adopted, and thus limit the number of particle trajectories that can be considered in a simulation. Nevertheless, an approach based on tracking individual particle trajectories provides a good approximation to MNP targeting and provides a useful tool for predicting particle distribution in vascular networks. Moreover, it yields simple analytical results that can be readily used to evaluate the targeting efficiency of various protocols. However, many works that adopt this approach make significant errors in interpreting their results and estimating targeting efficiency. In particular, it is common practice to assess targeting efficiency by starting with an homogeneous initial distribution of particles distributed across the entrance of the vessel network, and then measuring the fraction of these particles that end up being captured on the walls of the vessels as they pass through the network, see for example [29, 20, 27, 30, 2, 1, 31]. This does not provide a true picture of the process as can be seen by considering what happens in practice. In *in-vivo* application, MNPs are typically injected into a large vein, from where they are returned to the heart and lungs (where they mix with the blood), before entering the main arterial network via the aorta. In the large arteries, as discussed in [9], the effect of the targeting field on the MNPs is insignificant, and it is only once the MNPs reach the smaller vessels (small arteries and downwards), where flow speeds and vessel diameters are sufficiently small, that the targeting field is strong enough to significantly affect particle distribution across the vessel cross-section. Thus, a representative model for *in-vivo* targeting, which is nevertheless tractable, is to consider a network of small vessels starting from a small artery into which a well mixed dilute suspension of MNPs enters *continuously* in time. Similarly for most *in-vitro* experiments a well-mixed suspension of particles is injected into the entrance of the network of artificial vessels. Typical geometry of a phantom vessel network often used in *in vitro* experiments [29, 27, 20, 35] is shown in Figure 1. At the network entrance the flow is reasonably well-approximated as a Poissueille flow, and thus many more MNPs enter, per unit time and per unit area, into a portion of the network's entrance close to the centre of the inlet vessel than into a portion of the network's entrance lying close to the vessel wall. Accounting for this effect means that, when assessing targeting efficiency, particle trajectories starting close to the centre of the network entrance should be weighted more heavily than those starting close vessel wall. Notably this effect is missing from the assessments of targeting efficiency conducted in [29, 20, 27, 30, 2, 1] and the related modelling works [3, 10, 16, 31] in which all particle trajectories are weighted equally. The same argument also applies to theoretical treatments of the standard *in-vitro* experiments that are used to assess targeting efficiencies in phantom vessel networks [29, 27]. Finally, we note that there are some works that do properly account for this effect by using a particle conservation equation and imposing constant concentration at the network inlet, see for example [9, 26, 23, 6]. However, these works are all based on models that include the effects of (shear-induced) diffusion in the

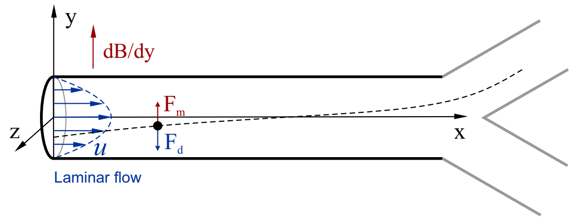

Figure 1: Geometry of the model. The channel has cylindrical geometry and a Poiseuille in-flow velocity profile, the magnetic field gradient is perpendicular to the flow. F_m and F_d are the magnetic and drag force acting on a magnetic particle.

particle conservation equation and it is wrongly believed that, where these diffusive effects can be neglected, formulation of the problem in terms of a conservation equation adds nothing to the understanding of the physics.

In what follows we present a 3D approach to modelling magnetically targeted delivery which is based on a conservation law for magnetic particles. Although this has extensive similarities with the simple particle tracking approach employed in other works it has the significant advantage that it allows the magnetic targeting efficiency to be computed correctly. We illustrate our approach in the simple vascular network shown in Figure 1 and use it to measure the targeting efficiency by calculating the fraction of the total particle flux that enters the (upper) targeted branch. A nice feature of performing this calculation in this geometry is that it is entirely analytic. However, the approach adopted here can equally be applied to more complex networks of vessels, albeit that the resulting calculations are computational rather than analytic. We model the targeting process by continuous injection of MNPs, at uniform concentration, into the entrance of the vessel network. This provides a much better way of assessing targeting efficiency, for both *in-vivo* magnetic targeting (in which the target particles are injected systemically) and for *in-vitro* magnetic targeting, than the alternative method which is based on tracking representative particles starting from their initial distribution. This is illustrated by the fact that it gives significantly better agreement to the *in-vitro* experimental results of Riegler *et al.* [29] than the alternative. We also show that another source of error, that leads to significant underestimation of targeting efficiency, occurs if the model is based on a single "representative" two-dimensional cross-section, of a three-dimensional vessel (as in [29, 20]).

In §2 we formulate a model, based on a conservation law for magnetic particles, for magnetic targeting in a vessel network. We show how this model is related to the particle trajectories and illustrate its use in the simple network, with a single bifurcation, depicted in Figure 1. We focus particularly on targeting efficiency and, by considering the particle flux division at the junction where the flow divides into the daughter vessels, we are able to derive an expression for targeting efficiency. In §3 we discuss our results in terms of the experimental results reported in [29] for a targeting experiment conducted in a simple network of this form. Finally, in §4, we summarise our results and present our conclusions.

2 Model of magnetic targeting

The phantom vessel geometry commonly used to assess magnetic targeting efficiency in *in-vitro* experiment is a symmetric Y-junction channel with cylindrical cross-section (see Figure 1). Magnetic gradient force is applied perpendicular to the axis of the main channel, which serves to drive the magnetic carrier particles towards one of the output branches (often called the targeting branch) [29, 20, 35]. The symmetry of the geometry means that the flow in the mother vessel splits evenly between the two daughter vessels, so that particles that arrive at the end of the mother vessel in its top half flow into the top daughter vessel while particles that arrive at the end of the mother vessel in its bottom half flow into the bottom daughter vessel. In order to calculate the targeting efficiency in this set up (*i.e.* the fraction of the particle flux entering the top daughter vessel) we thus need only to model the particle dynamics in the mother vessel. The modelled geometry is a cylindrical vessel of radius b and length L oriented along the

Table 1: Notation

L	Vessel length
b	Vessel radius
u_0	Maximal fluid flow velocity
u_{av}	Average fluid flow velocity
η	Fluid viscosity
a	Magnetic particle hydrodynamic radius
$\mathbf{B}$	Magnetic flux density
$\mathbf{F}_m$	Magnetic force action on a particle
$\mathbf{F}_f$	Hydrodynamic force action on a particle
$\boldsymbol{m}$	Particle magnetic moment
$\boldsymbol{v}_p$	Magnetic particle velocity
c	Magnetic particle concentration
$\boldsymbol{j}$	Magnetic particle flux density
x, y, z	Coordinates on particle trajectory
x_0, y_0, z_0	Initial particle position
$\tilde{x}, \tilde{y}, \tilde{z}$	Dimensionless coordinates
β_m	Dimensionless magnetic parameter
$\mathcal{Y}_1, \mathcal{Z}_1$	Coordinates of separation surface 1
$\mathcal{Y}_2, \mathcal{Z}_2$	Coordinates of separation surface 2
N_{tot}	Total number of particles
N_1	Number of particles reaching the upper (targeted) daughter vessel
n_1	Fraction of particles reaching the upper (targeted) daughter vessel
N_2	Number of particles reaching the vessel wall
n_1	Fraction of particles reaching the vessel wall
N_t	Number of targeted particles
n_1	Fraction of targeted particles

x axis. The model is based on the following assumptions: (i) the flow in the vessel has Poiseuille flow; (ii) there is a continuous inflow of magnetic particles with a uniform particle concentration c_0; (iii) the magnetic particles have permanent magnetic moments; (iv) magnetic field gradient is uniform across the vessel and oriented along the y axis; (v) dipole-dipole interactions between particles are neglected. With the possible exception of (v) these assumptions are directly applicable to the *in-vitro* experiments of [29, 20, 11, 35, 19]. *In vivo*, magnetic targeting occurs primarily in the small vessels (below 1mm in diameter), in which there is little or no pulsation, and so here the Poiseuille flow assumption (i) is justified. Assumption (iii) is valid for ferromagnetic particles as well as for superparamagnetic particles in a strong magnetic field, above the saturation point (such as would occur in an MRI). Assumption (iv) is generally correct in the case of MRI-guided magnetic targeting, as the magnetic gradient is created on a much larger scale in comparison to the vessel dimensions. With assumption (v) we neglect a process of particle cluster formation inside small vessels. However, the model can effectively describe the motion of particle aggregates by treating an aggregate as a single particle with an effective size and magnetic moment. It can also be easily generalised to describe aggregates of anisotropic shape [27, 21].

The motion of magnetic particles in the flow is governed by magnetic and hydrodynamic drag forces. The magnetic force acting on a particle in an applied magnetic field $\mathbf{B}$ is:

$$\mathbf{F}_m = (\boldsymbol{m} \cdot \nabla)\mathbf{B}, \tag{1}$$

where $\boldsymbol{m}$ is the particle magnetic moment. In the applications we consider (*e.g.* MRI targeting) it can be assumed that the particle magnetisation is saturated so that its magnetic moment is given by $\boldsymbol{m} = VM_s\mathbf{B}/|\mathbf{B}|$, where M_s is the saturation magnetisation and V is the volume of magnetic material in the particle. In the case of particle aggregates, V is the total volume of magnetic material in the cluster. In MRI experiments the gradient coils are rapidly switched on and off in order to avoid overheating; the fraction of time that the gradient coils are in the on state can be accounted for by multiplying the magnetic force (1) by a duty cycle parameter D_c [29, 22].

The hydrodynamic drag force can be written as the Stokes drag force for a sphere

$$\mathbf{F}_h = -6\pi\eta a(\boldsymbol{v}_p - \boldsymbol{u}), \tag{2}$$

where η is the fluid viscosity, $\boldsymbol{u}$ and $\boldsymbol{v}_p$ are the fluid and particle velocities, and a is the particle hydrodynamic radius. In the case of particle aggregates, the drag force can be generalised by introducing a shape factor. An elongated/asymmetric aggregate can also be described by using two or three shape factors [8].

The balance between these two forces defines the equilibrium particle speed as:

$$\boldsymbol{v}_p = \boldsymbol{u} + \boldsymbol{v}_m, \text{ where } \boldsymbol{v}_m = \frac{\mathbf{F}_m}{6\pi\eta a}. \tag{3}$$

The velocity of Poiseuille flow inside the mother vessel is:

$$\boldsymbol{u} = u_0 \left(1 - \frac{y^2 + z^2}{b^2}\right) \boldsymbol{e}_x, \tag{4}$$

where u_0 is the maximal fluid flow velocity in the centre of the vessel. For the cylindrical geometry, $u_0 = 2u_{av}$, where u_{av} is the average fluid flow velocity.

In order to track particle distribution (and particle flux) within a vessel network it is useful to formulate the problem in terms of average particle concentration $c(\boldsymbol{r}, t)$. Particles within the networks advect with the flow and in response to magnetic forces. They may also experience some diffusive motion due to shear induced motion caused by their interactions with the red blood cells [7, 4] (thermally activated diffusion is negligible). Here we neglect this effect, noting that it is usually relatively small in comparison to the advective terms [26]. Under these assumptions conservation of MNPs gives rise to the following advection equation for their concentration:

$$\frac{\partial c}{\partial t} + \nabla \cdot (\boldsymbol{v}_p c) = 0. \tag{5}$$

Here $\boldsymbol{v}_p$ is the particle velocity defined in (3). This equation can be rewritten in the form

$$\frac{\partial c}{\partial t} + c(\nabla \cdot \boldsymbol{v}_p) + (\boldsymbol{v}_p \cdot \nabla)c = 0, \tag{6}$$

Upon recalling that the flow is incompressible $\nabla \cdot \boldsymbol{u} = 0$ and making use of the assumption that magnetic force, and hence magnetic velocity $\boldsymbol{v}_m$, is spatially uniform, the second term in (6) can be seen to be zero so that the advection equation reduces to:

$$\frac{\partial c}{\partial t} + (\boldsymbol{v}_p \cdot \nabla)c = 0. \tag{7}$$

Note that even where the magnetic force is spatially nonuniform, the second term is usually much smaller than the third term [9], as the magnetic velocity is usually much weaker than the fluid flow, so that (7) is still a very good approximation to (6). In order to close the problem, in-flow conditions are required at the inlet of the network $\partial\Omega_{inlet}$ together with zero in-flow conditions on the walls of the vessel. The choice of the in-flow conditions plays a key role in the interpretation of the results of the model and the conditions appropriate to most *in-vitro* experimental set ups is that the concentration at the entrance to the inlet vessel is constant

$$c|_{\partial\Omega_{inlet}} = c_0, \tag{8}$$

which simulates the inflow of a well-mixed suspension of particles, concentration c_0, into the network. The inflow conditions on the walls of the vessel $\partial\Omega_{wall}$ state simply that on those sections of wall where the particle velocity $\boldsymbol{v}$ is directed into the flow that the particle concentration is zero, *i.e.*

$$c|_{\partial\Omega_{wall}} = 0 \qquad \text{if } \ \boldsymbol{v} \cdot \boldsymbol{n} < 0, \tag{9}$$

where $\boldsymbol{n}$ is the outward normal to the vessel.

The characteristics $\mathbf{x} = \mathbf{r}(t)$ of the advection equation (7) are given by the particle trajectories, and along these characteristics concentration of particle is constant. That is

$$\text{along the characteristic } \mathbf{x} = \mathbf{r}(t) \left\{ \begin{array}{l} d\mathbf{r}/dt = \boldsymbol{v} \\ dc/dt = 0 \end{array} \right. . \tag{10}$$

The condition (8) implies that $c = c_0$ along characteristics emanating from the entrance to the network $\partial\Omega_{inlet}$, while the condition (9) implies that $c = 0$ along characteristics that emanate from one of the vessel walls $\partial\Omega_{wall}$ [9]. The interior of the network is thus divided into regions in which $c = c_0$ and those in which $c = 0$ and these regions are divided by a separation surface which is defined by the particle trajectories.

We now focus on the particle trajectories, or equivalently the characteristics of the advection equation (7), and use these trajectories to derive the solution to (7). In particular, we show that it is possible to interpret the solution in terms of the flux of particles that are captured on the walls of the vessel network and the flux of particles that makes its way through the network without being captured by the targeting field.

The equations for the particle trajectories are:

$$\begin{aligned} \frac{dx}{dt} &= u = u_0\Big(1 - \frac{y^2+z^2}{b^2}\Big), \\ \frac{dy}{dt} &= v_m, \\ \frac{dz}{dt} &= 0, \end{aligned} \tag{11}$$

from which the particle trajectories can be obtained as:

$$\begin{aligned} x(t) &= u_0\Big(1 - \frac{y_0^2+z_0^2}{b^2}\Big)t - \frac{u_0 v_m y_0 t^2}{b^2} - \frac{u_0 v_m^2 t^3}{3b^2}, \\ y(t) &= y_0 + v_m t, \\ z(t) &= z_0, \end{aligned} \tag{12}$$

or in the non-parametric form as:

$$\left.\begin{aligned} x\frac{v_m}{u_0} &= (y - y_0)\Big(1 - \frac{z_0^2}{b^2}\Big) - \frac{y^3 - y_0^3}{3b^2} \\ z &= z_0 \end{aligned}\right\} \tag{13}$$

where $y_0 = y(0)$ and $z_0 = z(0)$ is the position of the particle, in the y–z plane, at the entrance to the mother vessel on $x(0) = 0$.

Figure 2(a) and (c) show trajectories of magnetic particles in the central plane ($z_0 = 0$) for two different values of v_m. The characteristic trajectories divide into three sets, (i) those below the blue curve that enter the lower daughter vessel in the main flow, (ii) those between the blue and red curves that enter the upper daughter vessel in the main flow and (iii) those above the red curve that hit the wall of the mother vessel before the junction with the two daughter vessels. In terms of the *in-vitro* experiment MNPs flowing along both sets of characteristics (ii) and (iii) usually end up in the (upper) targeted daughter vessel, although those flowing along characteristics in set (iii) roll along the upper surface of the mother vessel before reaching the junction and entering the targeted daughter vessel.

2.1 Separation surfaces

Here we derive formulae for the surfaces that separate regions of the particle flow that enter the upper targeted vessel from those that end up on the walls of the mother vessel and from those that enter the lower untargetted vessel. For simplicity, we introduce dimensionless coordinates in equation (13) for the characteristics (*i.e.* particle trajectories), defined by

$$\tilde{x} = \frac{x}{L}, \quad \tilde{y} = \frac{y}{b}, \quad \tilde{z} = \frac{z}{b}.$$

Thus, where $0 \le \tilde{x} \le 1$ and $\tilde{y}^2 + \tilde{z}^2 \le 1$, these trajectories remain within the domain of interest (*i.e.* the mother vessel). Under this rescaling the two parameter family of characteristics defined in (13) transform to

$$\left.\begin{aligned} \tilde{x}\beta_m &= (\tilde{y} - \tilde{y}_0)(1 - \tilde{z}_0^2) - \frac{\tilde{y}^3 - \tilde{y}_0^3}{3} \\ \tilde{z} &= \tilde{z}_0 \end{aligned}\right\} \tilde{y}_0^2 + \tilde{z}_0^2 \le 1, \tag{14}$$

where β_m is the dimensionless magnetic targeting parameter defined by

$$\beta_m = \frac{v_m}{u_0}\frac{L}{b}. \tag{15}$$

Separation surface 1. In the experimental configuration considered here, the fluid flow at the end of the mother vessel divides equally between the two daughter vessels. Streamlines that reach the end of the mother vessel (at $\tilde{x} = 1$) below the line $\tilde{y} = 0$ flow into the lower (untargetted) daughter vessel while those that reach $\tilde{x} = 1$ above the line $\tilde{y} = 0$ flow into the upper (targetted) daughter vessel. Near the end of the mother vessel, close to the bifurcation, the

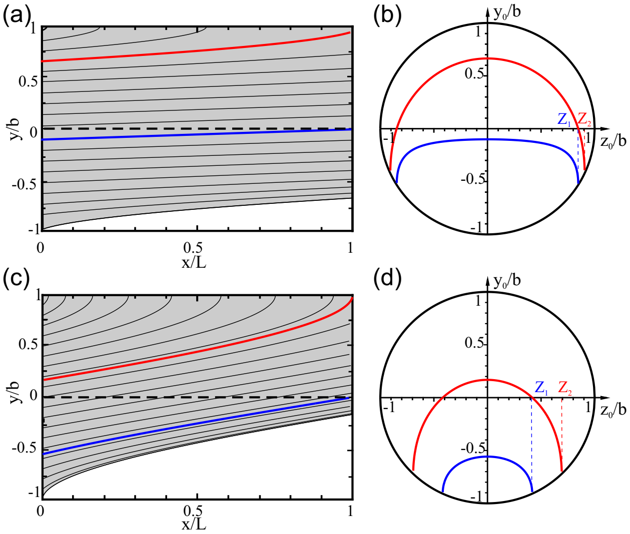

Figure 2: (a) (c) Trajectories of magnetic particles at the central plane ($z_0 = 0$) calculated using Equation (14) for $\beta_m = \dfrac{v_m}{u_0}\dfrac{L}{b} = 0.1$ and 0.5, respectively. The shaded regions show area where $c = c_0$, while in white regions $c = 0$. All the characteristic trajectories below the blue line enter the lower (non-targeted) vessel; all characteristics above the red line reach the vessel wall before the bifurcation, while only those between the red and blue lines enter the upper (targeted) vessel in the main flow. (b) (d) Show the separation surfaces at the entrance to the mother vessel. Particles entering between the blue and red curves reach the upper (targeted) daughter vessel in the main flow, those above the red curve end up hitting the wall of the mother vessel (and may either stick to it or propagate along the wall depending on its properties) whilst those below the blue curve enter the lower daughter vessel. The intersection of the separation surfaces with the entrance are defined by $\mathcal{Y}_1 = \mathcal{Y}_1(\tilde{z}_0)$ and $\mathcal{Y}_2 = \mathcal{Y}_2(\tilde{z}_0)$ (blue and red curves, respectively) by Equations (16) and (19) and calculated for $\beta_m = 0.1$ and 0.5, respectively.

flow is fully three-dimensional (*i.e.* the Poiseuille flow approximation no longer holds). However this deviation from Poiseuille flow only occurs over a region of (dimensional) size $O(b)$ from the bifurcation and so, given that the (dimensional) length of the vessel L is much greater than its width b, the magnetic force is not strong enough to significantly alter the particle trajectories within this region. Thus, to a good approximation, particles that reach $\tilde{x} = 1$ (the end of the Poiseuille flow region in the mother vessel) below the line $\tilde{y} = 0$ flow into the lower (untargetted) daughter vessel, while those that reach it above the line $\tilde{y} = 0$ flow into the upper (targetted) daughter vessel. In order to see which of the particle trajectories entering the mother vessel flow into the (upper) targeted vessel and which flow into the (lower) untargeted vessel, we seek to map the dividing line $(\tilde{x}, \tilde{y}) = (1, 0)$ back to the surface $\tilde{x} = 0$. Parametrising the dividing line $(\tilde{x}, \tilde{y}) = (1, 0)$ by $\tilde{z} = \tilde{z}_0$ and denoting its map back onto the surface $\tilde{x} = 0$ by the function $\tilde{y} = \mathcal{Y}_1(\tilde{z}_0)$, we find, using (14), that $\mathcal{Y}_1(\tilde{z}_0)$ satisfies the implicit equation

$$\frac{\mathcal{Y}_1^3(\tilde{z}_0)}{3} - (1 - \tilde{z}_0^2)\mathcal{Y}_1(\tilde{z}_0) - \beta_m = 0. \qquad (16)$$

Another way of thinking of the curve $\tilde{y} = \mathcal{Y}_1(\tilde{z}_0)$ is as the intersection of the surface that separates particle trajectories entering the upper and lower vessels with the entrance to the mother vessel. Examples of this curve are shown by the blue curves in Figures 2(b) and (d). Particle trajectories entering the mother vessel below the blue curves end up entering the lower (untargetted) vessel, while those entering above the blue curve either end up on the wall of the mother vessel or entering the upper (targetted) vessel.

Notably (16) does not have solutions for all $\tilde{z}_0$ in the range $-1 \leq \tilde{z}_0 \leq 1$. The solutions only exist for $\tilde{z}_0$ in the range

$$-\mathcal{Z}_1 \leq \tilde{z}_0 \leq \mathcal{Z}_1 \text{ where } \mathcal{Z}_1 = \sqrt{1 - \left(\frac{3}{2}\beta_m\right)^{2/3}}, \qquad (17)$$

It follows that there are no solutions, for any $\tilde{z}_0$, if

$$\beta_m \geq \frac{2}{3}. \qquad (18)$$

Physically this condition corresponds to magnetic forces that are sufficiently strong to ensure that no particle trajectories entering the mother vessel at $\tilde{x} = 0$ are able to reach the lower (untargeted) daughter vessel.

Separation surface 2. The second separation surface divides characteristics (particle trajectories) that end up on the wall of the mother vessel from those that enter the upper (targetted) vessel in the main flow. The terminal points for the characteristics on this separation surface lie on the curve segment $(\tilde{x} = 1,\ \tilde{y} = \sqrt{1-\tilde{z}_0^2},\ \tilde{z} = \tilde{z}_0)$ where $-1 \leq \tilde{z}_0 \leq 1$, *i.e.* the upper half of the vessel wall at the exit to the mother vessel. An algebraic relation $\tilde{y} = \mathcal{Y}_2(\tilde{z}_0)$ for the curve formed by the intersection of this family of characteristics with the entrance to the mother vessel $\tilde{x} = 0$ can be determined from (14) and is readily shown to be

$$\frac{\mathcal{Y}_2^3}{3} - \mathcal{Y}_2(1-\tilde{z}_0^2) + \frac{2}{3}(1-\tilde{z}_0^2)^{3/2} - \beta_m = 0. \qquad (19)$$

Examples of this curve are shown in Figure 2(b) and (d) in red. Particle trajectories entering the mother vessel above these red curves end up on the (upper) wall of the mother vessel while those that enter the mother vessel below these curves enter the daughter vessels in the main flow.

It is readily shown that (19) only has solutions for $\tilde{z}_0$ in the range

$$-\mathcal{Z}_2 \leq \tilde{z}_0 \leq \mathcal{Z}_2 \text{ where } \mathcal{Z}_2 = \sqrt{1-\left(\frac{3}{4}\beta_m\right)^{2/3}}, \quad (20)$$

In particular for sufficiently strong magnetic forces, such that

$$\beta_m \geq \frac{4}{3}, \qquad (21)$$

there are no solutions to this equation at all, a consequence of all particle trajectories entering the mother vessel (at $\tilde{x} = 0$) ending up on the upper surface of the mother vessel before the junction with the daughter vessels.

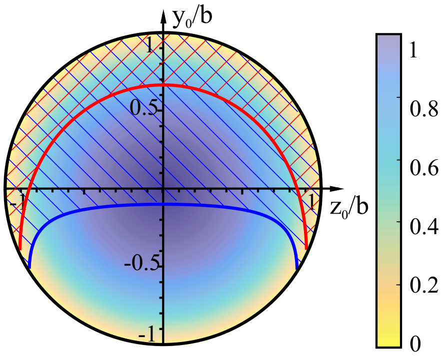

Figure 3: Colourmap shows normalized particle flux density at the entrance of the mother vessel. Particles flowing into the mother vessel between the red and blue curves enter the upper (targeted) daughter vessel in the main flow. Blue and red curves show $\tilde{y} = \mathcal{Y}_1(\tilde{z}_0)$ and $\tilde{y} = \mathcal{Y}_2(\tilde{z}_0)$, the intersection of the separation surfaces with $\tilde{x} = 0$, the entrance to the mother vessel (as defined in (16) and (19)) and calculated for $\beta_m = 0.1$. The corresponding areas of integration for N_1 and N_2, $\mathcal{S}_1$ and $\mathcal{S}_2$, are shown by blue and red hatched regions.

2.2 Targeting efficiency

A key part of this analysis is to calculate (i) the total flux of particles reaching the lower (untargetted) daughter vessel, (ii) the total flux of particles reaching the upper (targetted) daughter vessel in the main flow and (iii) the total flux of particles reaching the upper wall of the mother vessel. In terms of the *in-vitro* experiment it is usually the case that particles that reach the upper wall of the mother vessel continue to flow/roll along the wall of this vessel until they enter the daughter vessel and so, when the method for assessing targeting efficiency is simply to measure fraction of particles that come out of the upper vessel as a ratio of those that enter the mother vessel, we can identify (ii) and (iii) as the targetted fluxes. In order to assess the targeting efficiency, via the calculation of these fluxes, we consider the conservation equation for magnetic particle transport through the network, as provided by (7), and identify the particle flux density as $\mathbf{j} = c\boldsymbol{v}_p$. We assume that the flow and magnetic field are steady and that particles are fed into the network at the entrance to the mother vessel at a uniform concentration c_0. Since this is a steady problem, (7) implies that the flux of particles entering a given region is equal to the flux leaving that region. It follows that the total flux of particles that enters (i) the lower (untargetted) daughter vessel is equal to the total flux of particles entering the mother vessel below separation surface 1, whose intersection with the entrance to the mother vessel is given by $\tilde{y} = \mathcal{Y}_1(\tilde{z}_0)$, where $\mathcal{Y}_1(\tilde{z}_0)$ satisfies (16).

Notably the flux density of particles $\mathbf{j}\cdot\hat{\boldsymbol{n}}|_{\mathcal{S}_0}$ flowing in through the entrance to mother vessel, $\mathcal{S}_0$ (here $\hat{\boldsymbol{n}} = \boldsymbol{e}_x$ is the unit inward normal to $\mathcal{S}_0$) is not uniform in space but has a parabolic Poiseuille profile (shown in Figure 3), that is

$$\mathbf{j}\cdot\hat{\boldsymbol{n}}|_{\mathcal{S}_0} = c_0\boldsymbol{u}\cdot\boldsymbol{e}_x|_{\mathcal{S}_0} = c_0u_0(1-\tilde{y}_0^2-\tilde{z}_0^2). \tag{22}$$

In particular, the particle flux density near the centre of the vessel is much greater than that near its edges, a fact that is not accounted for in the calculations of targeting efficiency made in [29, 20, 27, 30] and which leads to the error in these calculations.

In order to calculate the total particle flux leaving the vessel through a particular surface $\mathcal{A}$, we can use the characteristic trajectories (particle paths) to map the area $\mathcal{A}$ back to a surface on the entrance of the mother vessel, $\mathcal{A}_0$. As noted earlier, since this is a steady problem and particles are conserved, $N_{\mathcal{A}}$ the total flux of particles through $\mathcal{A}$, is equal to the total flux of particles flowing through $\mathcal{A}_0$. It follows that

$$N_{\mathcal{A}} = \iint_{\mathcal{A}_0} c_0\boldsymbol{v}_p\cdot\hat{\boldsymbol{n}}\,dS = c_0u_0\iint_{\mathcal{A}_0}(1-\tilde{y}_0^2-\tilde{z}_0^2)\,d\tilde{y}_0d\tilde{z}_0 \tag{23}$$

This can be compared to N_{tot}, the total flux of particles entering the network, which is obtained by integration over the whole input area $\mathcal{S}_0$:

$$N_{tot} = c_0u_0\iint_{\mathcal{S}_0}(1-\tilde{y}_0^2-\tilde{z}_0^2)\,d\tilde{y}_0d\tilde{z}_0 = c_0u_0\frac{\pi}{2}. \tag{24}$$

In order to calculate N_1, the sum of fluxes of particles entering the targeted daughter vessel (case (ii) above) and reaching the upper wall of the mother vessel (case (iii) above), we compute the integral of the flux density $\mathbf{j}\cdot\hat{\boldsymbol{n}}$ above the first separation surface $\tilde{y} = \mathcal{Y}_1(\tilde{z}_0)$ (area $\mathcal{S}_1$ is shown by the blue hatched region in Figures 3); that is

$$N_1 = c_0u_0\iint_{\mathcal{S}_1}(1-\tilde{y}_0^2-\tilde{z}_0^2)\,d\tilde{y}_0d\tilde{z}_0. \tag{25}$$

Similarly N_2, the total flux of particles onto the upper wall of the mother vessel (case (iii) above), is computed from the integral of the flux density $\mathbf{j}\cdot\hat{\boldsymbol{n}}$ above the second separation surface $\tilde{y} = \mathcal{Y}_2(\tilde{z}_0)$ (area $\mathcal{S}_2$ is shown by the red hatched region in Figures 3); that is

$$N_2 = c_0u_0\iint_{\mathcal{S}_2}(1-\tilde{y}_0^2-\tilde{z}_0^2)\,d\tilde{y}_0d\tilde{z}_0. \tag{26}$$

The corresponding fraction of the total particle fluxes, as defined by $n_1 = N_1/N_{tot}$ and $n_2 = N_2/N_{tot}$, are given by the expressions:

$$\begin{aligned} n_1 =& 1 + \left(\frac{3\beta_m}{\pi} - \frac{1}{\pi}\left(\frac{3\beta_m}{2}\right)^{1/3}\right)\sqrt{1-\left(\frac{3\beta_m}{2}\right)^{2/3}} \\ & - \frac{1}{\pi}\sin^{-1}\sqrt{1-\left(\frac{3\beta_m}{2}\right)^{2/3}}, \end{aligned} \tag{27}$$

$$\begin{aligned} n_2 =& 1 + \left(\frac{3\beta_m}{\pi} - \frac{2}{\pi}\left(\frac{3\beta_m}{4}\right)^{1/3}\right)\sqrt{1-\left(\frac{3\beta_m}{4}\right)^{2/3}} \\ & - \frac{2}{\pi}\sin^{-1}\sqrt{1-\left(\frac{3\beta_m}{4}\right)^{2/3}}. \end{aligned} \tag{28}$$

The dependence of n_1 and n_2 on parameter β_m is plotted in Figure 4. The fractions n_1 and n_2 reach 1 at $\beta_m = 2/3$ and $\beta_m = 4/3$, respectively, as shown in Equations (18) and (21).

The treatment described here is not limited to a particular type of particle-wall interaction. In order to illustrate this, we consider two extreme cases: firstly the case where the targetted particles stick to the vessel wall when they reach it; and secondly the case where the particles do not stick to the vessel wall when they come in contact with it, but instead continue to flow/roll along the wall, in the direction

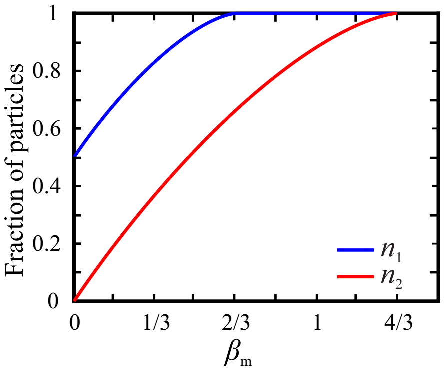

Figure 4: Dependence of particle fraction n_1 and n_2 on β_m given by Equations (27) and (28), respectively.

of the flow, until they enter the upper (targetted) daughter vessel. In the first case, the fraction of the particle flux that enters the upper (targetted) daughter vessel is $n_t = n_1 - n_2$, while the fraction of particle flux deposited on the wall of the mother vessel is $n_d = n_2$. In the second case, particles do not deposit on the vessel walls and thus the fraction of the total particle flux entering the upper daughter vessel is $n_t = n_1$. In the real system, only a fraction of particles that approach the sidewall will stick to it. More precise particle-wall interaction models can be found in [23, 34].

In the *in-vitro* experimental works [29, 27], targeting efficiency is measured by the parameter $T_e = 2(N_t/N_{tot} - 0.5)$, where N_t is the number of particles that reach the upper (targetted) vessel, and N_{tot} is the total number of particles entering the mother vessel. In terms of these definitions we can identify N_t/N_{tot} as n_1, and it follows (on using (27)) that our model determines this measure of targetting efficiency as

$$T_e = 1 + \left(\frac{6\beta_m}{\pi} - \frac{2}{\pi}\left(\frac{3\beta_m}{2}\right)^{1/3}\right)\sqrt{1-\left(\frac{3\beta_m}{2}\right)^{2/3}} - \frac{2}{\pi}\sin^{-1}\sqrt{1-\left(\frac{3\beta_m}{2}\right)^{2/3}}, \tag{29}$$

where β_m is defined in (15). Plots of our theoretical results for T_e (red curve) are compared to the experimental results of [29] (black symbols) and to their theoretical results (blue dashed curve) in Figure 5.

3 Discussion

In Figure 5 we compare the result of our magnetic targeting model (29) to the *in-vitro* experimental data from [29], and show that with the correct interpretation of targeting efficiency (solid red curves) there is good qualitative agreement to the experimental data. Furthermore, the agreement obtained here is around an order magnitude better than the incorrect model interpretation proposed in [29] (dashed blue curves). Nevertheless there is still around a factor of two discrepancy between our model and the experiment. We believe that this discrepancy can be explained by small aggregations of cells occurring, as a consequence of magnetic chaining effects, over the course of the experiment. Since these aggregates are larger than the individual cells (on which the model is based), they are targeted more effectively, and this explains why the theory underestimate the experimental targeting efficiency. It is noticeable that with the incorrect interpretation of the theory the targeting efficiency predictions are more than a factor of 10 below the experimental ones. For example, for BioMag-labelled cells at flow velocity of 1 cm/s, the experimental targeting efficiency is 49%, and with our corrected model interpretation we obtain 29%, while the erroneous model interpretation in [29] predicts only 4%. This is important because the authors of [29] use their results to infer a very high level of cell aggregation whereas we believe the level of aggregation to be much lower. Following [29], we use the number of cells per aggregate as a fitting parameter and find the best agreement between our model and the experiment (shown by green dashed lines in Figure 5) is found where there are 3 to 4 cells per aggregate. This contrasts with the results of [29], where the best agreement between model and experiment is obtained for 30-40 cells per aggregate.

There are two main differences between our analysis and that in [29], which explain why our results give

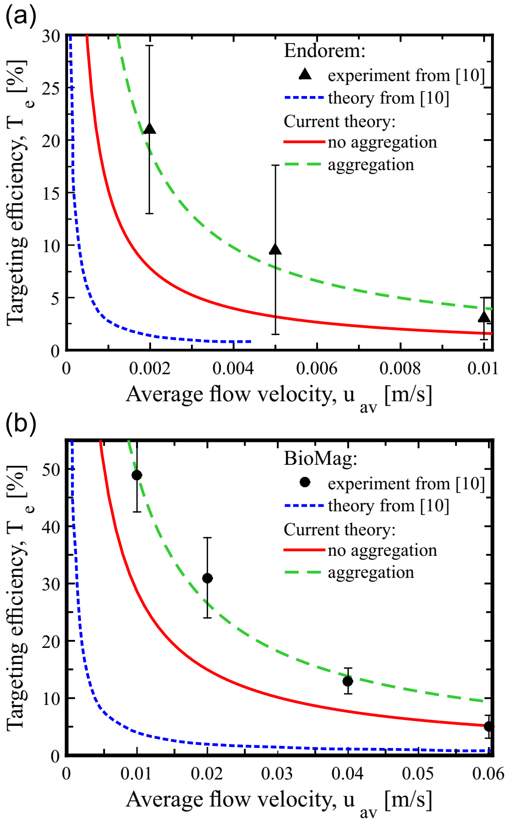

Figure 5: Targeting efficiency depending on the flow rate or cells labelled with (a) Endorem and (b) BioMag particles. Points are experimental data from [29]; dotted lines are theoretical results from [29]; solid lines are theoretical results calculated using Equation (29) and experimental parameters from Table 2 and assuming no cell aggregation; dashed lines are theoretical results assuming that there are on average 4 and 3 cells per aggregate for Endorem and BioMag particles, respectively. Notice that the theory described here is within a factor of 2 of the experimental results (without invoking cell aggregation) while the theory given in [29] is an order of magnitude out.

Table 2: Parameters of experiment [29]

Channel length, L [m]	0.06
Channel radius, b [m]	0.4×10^{-3}
Cell radius, a [m]	5×10^{-6}
Average fluid velocity, u_{av} [m/s]	0.001 to 0.06
Fluid viscosity, η [kg/m/s]	1.6×10^{-3}
Magnetic gradient, dB/dy [T/m]	0.5
MRI duty cycle parameter, D_c	2/7
Saturation magnetization, M_s [A/m]	314×10^{3}

significantly higher targeting efficiency that are more in line with the experimental data. The main difference comes from the fact that the model formulated in [29] does not consider the particle flux distribution associated with the particle trajectories (characteristics) when calculating targeting efficiency. Indeed, they assume that all trajectories should be weighted equally. However, as discussed above, this is incorrect, and leads to a significant underestimation of targeting efficiency. In addition, the model used in [29] is two-dimensional, and only considers the central ($z_0 = 0$) plane. The circular flow profile is accounted for by introducing a heuristic weighting factor [20, 27]. However, as can be seen from Figure 3, the fraction of targeted particles is lowest in the central plane, as the flow velocity is the highest there, and so it provides a poor picture of targeting across the entirety of the cylindrical vessel.

Details of experiment in [29]. The data collected in [29] comes from experiments in which human mononuclear cells labelled with commercially available superparamagnetic iron oxide nanoparticles Endorem (Guerbet Laboratories Ltd, UK) and BioMag (Bangs Laboratories Inc, IN, USA) were targeted in the phantom vessel geometry described above (see figure 1) in an MRI scanner. The amount of internalized iron per cell of Endorem and BioMag was 15 and 295 pg/cell, respectively. All other experimental parameters are given in Table 2.

e

4 Summary and Conclusions

We have presented a model, based on a particle conservation law, that is capable of accurately predicting magnetic targeting and targeting efficiency in a flow through a network of vessels. We have illustrated its use in a simple network, with a single bifurcation, that is commonly used in *in-vitro* investigation of magnetic targeting. In this context, we were able to derive an analytic expression for the targeting efficiency, *i.e.* the fraction of the magnetic particle flux entering the mother vessel that flows into the targeted daughter vessel. Our analysis corrects a common error that is made in assessing the efficiency of magnetic targeting, and that occurs widely through the literature [29, 20, 27, 30, 2, 1, 3, 10, 16, 31]. Furthermore, we have demonstrated that the corrected theory shows much better agreement to *in-vitro* experimental results [29] than does the erroneous method. This error arises because of a failure to correctly weight particle trajectories entering the vessel network. In particular, particle trajectories entering near the center of the mother vessel (where the flow is fast) are associated with a correspondingly larger particle flux than trajectories that enter near the edge of the mother vessel (where the flow is slow) and so their effects need to be weighted accordingly. The methods presented here can readily be extended to more complex geometries and pave the way for accurate numerical simulations of targeting in realistic vascular networks.

Finally, we remark that in magnetic targeting *in-vivo* it may be necessary, depending upon the vessel size and its position in the network, to account for shear-induced diffusion [26, 23, 6] arising from the interaction of the magnetic particles with red blood cells and for the non-Newtonian rheology of blood [6]. We note that continuum models that include shear-induced diffusion have been analysed in [26] but that there is considerable uncertainty as to how to correctly account for this effect. A key feature, predicted by the solutions of such models, is a diffusion boundary layer around the edge of the vessel, in which a balance is established between the magnetic force pulling particles onto the wall and diffusion which acts to redistribute them. However, it is in these regions that the Fåhraeus–Lindqvist effect manifests itself in the form of a red-blood cell depleted layer. The lack of red-blood cells around the vessel walls complicates the modelling because it leads to reduced shear-induced diffusion in the boundary layer and thus alters the behaviour of the solution there. A microscopic treatment of these phenomena, which is particularly pertinent in the smaller vessels, is given in [7] in which the motion of magnetic particles interacting with discrete red-blood cells, and subject to an external magnetic force, are investigated.

Acknowledgments

The authors would like to acknowledge the financial support from the research project ”Magnetic delivery of anti-cancer magnetosomes using MRI” funded by Cancer Research UK.

References

[1] M. Avilés, E. A.D., and J. A. Ritter. Implant assisted-magnetic drug targeting: comparison of in vitro experiments with theory. *Journal of Magnetism and Magnetic Materials*, 320:2704–2713, 2008.

[2] H. Chen, A. D. Ebner, M. D. Kaminski, A. J. Rosengart, and J. A. Ritter. Analysis of magnetic drug carrier particle capture by a magnetizable intravascular stent—2: Parametric study with multi-wire two-dimensional model. *Journal of Magnetism and Magnetic Materials*, 293:616–632, 2005.

[3] H. Chen, M. D. Kaminski, and A. J. Rosengart. 2d modeling and preliminary in vitro investigation of a prototype high gradient magnetic separator for biomedical applications. *Medical engineering & physics*, 30(1):1–8, 2008.

[4] E. M. Cherry and J. K. Eaton. A comprehensive model of magnetic particle motion during magnetic drug targeting. *International Journal of Multiphase Flow*, 59:173–185, 2014.

[5] J. Dobson. Magnetic nanoparticles for drug delivery. *Drug Development Research*, 67:55–60, 2006.

[6] C. Fanelli, K. Kaouri, T. Phillips, T. Myers, and F. Font. Magnetic nanodrug delivery in non-newtonian blood flows. arXiv:2102.03911v2.

[7] J. B. Freund and B. Shapiro. Transport of particles by magnetic forces and cellular blood flow in a model microvessel. *Physics of Fluids*, 24(5):051904, 2012.

[8] A. S. Geller, L. A. Mondy, D. J. Rader, and M. S. Ingber. Boundary element method calculations of the mobility of nonspherical particles - 1. linear chains. *Journal of Aerosol Science*, 24(5):597–609, 1993.

[9] A. D. Grief and G. Richardson. Mathematical modelling of magnetically targeted drug delivery. *Journal of Magnetism and Magnetic Materials*, 293(1):455 – 463, 2005. Proceedings of the Fifth International Conference on Scientific and Clinical Apllications of Magnetic Carriers.

[10] J. W. Haverkort, S. Kenjereš, and C. R. Kleijn. Computational simulations of magnetic particle capture in arterial flows. *Annals of Biomedical Engineering*, 37(12):2436–2448, 2009.

[11] A. K. Hoshiar, T.-A. Le, F. U. Amin, M. O. Kim, and J. Yoon. A novel magnetic actuation scheme to disaggregate nanoparticles and enhance passage across the blood – brain barrier. *Nanomaterials*, 8(1), 2018.

[12] E. G. Karvelas, N. K. Lampropoulos, and I. E. Sarris. A numerical model for aggregations formation and magnetic driving of spherical particles based on OpenFOAM®. *Computer Methods and Programs in Biomedicine*, 142:21–30, 2017.

[13] S. D. Kong, J. Lee, S. Ramachandran, B. P. Eliceiri, V. I. Shubayev, R. Lal, and S. Jin. Magnetic targeting of nanoparticles across the intact blood-brain barrier. *Journal of Controlled Release*, 164(1):49–57, 2012.

[14] P. G. Kyrtatos, P. Lehtolainen, M. Junemann-Ramirez, A. Garcia-Prieto, A. N. Price, J. F. Martin, D. G. Gadian, Q. A. Pankhurst, and M. F. Lythgoe. Magnetic Tagging Increases Delivery of Circulating Progenitors in Vascular Injury. *JACC: Cardiovascular Interventions*, 2(8):794–802, aug 2009.

[15] A. S. Lübbe, C. Bergemann, H. Riess, F. Schriever, P. Reichardt, K. Possinger, M. Matthias, B. Dörken, F. Herrmann, R. Gürtler, P. Hohenberger, N. Haas, R. Sohr, B. Sander, A.-J. Lemke, D. Ohlendorf, W. Huhnt, and D. Huhn. Clinical experiences with magnetic drug targeting: A phase I study with 4'-epidoxorubicin in 14 patients with advanced solid tumors. *Cancer Research*, 56(20):4686–4693, 1996.

[16] T. Lunnoo and T. Puangmali. Capture Efficiency of Biocompatible Magnetic Nanoparticles in Arterial Flow: A Computer Simulation for Magnetic Drug Targeting. *Nanoscale Research Letters*, 10(1), 2015.

[17] H. Maeda, H. Nakamura, and J. Fang. The EPR effect for macromolecular drug delivery to solid tumors: Improvement of tumor uptake, lowering of systemic toxicity, and distinct tumor imaging in vivo. *Advanced drug delivery reviews*, 65(1):71–79, 2013.

[18] M. K. D. Manshadi, M. Saadat, M. Mohammadi, M. Shamsi, M. Dejam, R. Kamali, and A. Sanati-Nezhad. Delivery of magnetic micro/nanoparticles and magnetic-based drug/cargo into arterial flow for targeted therapy. *Drug Delivery*, 25(1):1963–1973, 2018. PMID: 30799655.

[19] J.-B. Mathieu and S. Martel. Magnetic microparticle steering within the constraints of an MRI system: proof of concept of a novel targeting approach. *Biomedical microdevices*, 9(6):801–808, 2007.

[20] J.-B. Mathieu and S. Martel. Steering of aggregating magnetic microparticles using propulsion

gradients coils in an MRI scanner. *Magnetic Resonance in Medicine*, 63(5):1336–1345, 2010.

[21] L. Mellal, K. Belharet, D. Folio, and A. Ferreira. Optimal structure of particles-based superparamagnetic microrobots: application to MRI guided targeted drug therapy. *Journal of Nanoparticle Research*, 17(2):64, 2015.

[22] M. Muthana, A. J. Kennerley, R. Hughes, E. Fagnano, J. Richardson, M. Paul, C. Murdoch, F. Wright, C. Payne, M. F. Lythgoe, N. Farrow, J. Dobson, J. Conner, J. M. Wild, and C. Lewis. Directing cell therapy to anatomic target sites in vivo with magnetic resonance targeting. *Nature Communications*, 6:1–11, 2015.

[23] A. Nacev, C. Beni, O. Bruno, and B. Shapiro. The behaviors of ferromagnetic nano-particles in and around blood vessels under applied magnetic fields. *Journal of Magnetism and Magnetic Materials*, 323(6):651–668, 2011.

[24] Q. A. Pankhurst, J. Connolly, S. Jones, and J. Dobson. Applications of magnetic nanoparticles in biomedicine. *Journal of physics D: Applied physics*, 36(13):R167, 2003.

[25] P. Pouponneau, J. C. Leroux, G. Soulez, L. Gaboury, and S. Martel. Co-encapsulation of magnetic nanoparticles and doxorubicin into biodegradable microcarriers for deep tissue targeting by vascular MRI navigation. *Biomaterials*, 32(13):3481–3486, 2011.

[26] G. Richardson, K. Kaouri, and H. M. Byrne. Particle trapping by an external body force in the limit of large peclet number: applications to magnetic targeting in the blood flow. *European Journal of Applied Mathematics*, 21(1):77–107, 2010.

[27] J. Riegler, B. Allain, R. J. Cook, M. F. Lythgoe, and Q. A. Pankhurst. Magnetically assisted delivery of cells using a magnetic resonance imaging. *Journal of Physics D: Applied Physics*, 44:055001, 2011.

[28] J. Riegler, A. Liew, S. O. Hynes, D. Ortega, T. O. Brien, R. M. Day, T. Richards, F. Sharif, Q. A. Pankhurst, and M. F. Lythgoe. Superparamagnetic iron oxide nanoparticle targeting of MSCs in vascular injury. *Biomaterials*, 34(8):1987–1994, 2013.

[29] J. Riegler, J. A. Wells, P. G. Kyrtatos, A. N. Price, Q. A. Pankhurst, and M. F. Lythgoe. Targeted magnetic delivery and tracking of cells using a magnetic resonance imaging system. *Biomaterials*, 31(20):5366–5371, 2010.

[30] J. A. Ritter, A. D. Ebner, K. D. Daniel, and K. L. Stewart. Application of high gradient magnetic separation principles to magnetic drug targeting. *Journal of Magnetism and Magnetic Materials*, 280:184–201, 2004.

[31] F. Russo, A. Boghi, and F. Gori. Numerical simulation of magnetic nano drug targeting in patient specific lower respiratory tract. *Journal of Magnetism and Magnetic Materials*, 451:554–564, 2018.

[32] M. Shamsi, A. Sedaghatkish, M. Dejam, M. Saghafian, M. Mohammadi, and A. Sanati-Nezhad. Magnetically assisted intraperitoneal drug delivery for cancer chemotherapy. *Drug Delivery*, 25(1):846–861, 2018. PMID: 29589479.

[33] B. Shapiro, S. Kulkarni, A. Nacev, S. Muro, P. Y. Stepanov, and I. N. Weinberg. Open challenges in magnetic drug targeting. *Wiley Interdisciplinary Reviews: Nanomedicine and Nanobiotechnology*, 7(3):446–457, 2015.

[34] K. Talaska and A. Ferreira. An approach to identifying phenomena accompanying micro and nanoparticles in contact with irregular vessel walls. *IEEE Transactions on Nanobioscience*, 16(6):463–475, 2017.

[35] P. Vartholomeos and C. Mavroidis. In silico studies of magnetic microparticle aggregations in fluid environments for MRI-guided drug delivery. *IEEE Transactions on Biomedical Engineering*, 59(11):3028–3038, 2012.